metals

MDPI

Article

Precipitation Behavior of Carbides in H13 Hot Work Die Steel and Its Strengthening during Tempering

Angang Ning [1], Wenwen Mao [2], Xichun Chen [3], Hanjie Guo [2,*] and Jing Guo [2]

1 School of Material Science and Engineering, Taiyuan University of Technology, Taiyuan 030024, China; ningangang1986@163.com
2 School of Metallurgical and Ecological Engineering, University of Science and Technology Beijing, Beijing 100083, China; hrc7087097@163.com (W.M.); guojingzq@163.com (J.G.)
3 Department of High Temperature Materials, Central Iron and Steel Research Institute, Beijing 100094, China; chenxichun@189.cn
* Correspondence: guohanjie@ustb.edu.cn; Tel.: +86-10-6233-4964

Academic Editor: Robert Tuttle
Received: 6 December 2016; Accepted: 18 February 2017; Published: 23 February 2017

Abstract: The properties of carbides, such as morphology, size, and type, in H13 hot work die steel were studied with optical microscopy, transmission electron microscopy, electron diffraction, and energy dispersive X-ray analysis; their size distribution and quantity after tempering, at different positions within the ingot, were analyzed using Image-Pro Plus software. Thermodynamic calculations were also performed for these carbides. The microstructures near the ingot surface were homogeneous and had slender martensite laths. Two kinds of carbide precipitates have been detected in H13: (1) MC and M_6C, generally smaller than 200 nm; and (2) $M_{23}C_6$, usually larger than 200 nm. MC and M_6C play the key role in precipitation hardening. These are the most frequent carbides precipitating at the halfway point from the center of the ingot, and the least frequent at the surface. From the center of the ingot to its surface, the size and volume fraction of the carbides decrease, and the toughness improves, while the contribution of the carbides to the yield strength increases.

Keywords: H13 steel after tempering; thermodynamic calculation; carbides; precipitation strengthening

1. Introduction

As a typical hot work die steel, H13 (4Cr5MoSiV1) (where "4" means that the carbon content is about 0.4%), has excellent resistance to heat, wear, and thermal mechanical fatigue [1]; thus, it is widely employed in high temperature applications, such as die casting molds, hot rolling, hot extrusion, and hot forging, where the operating tool is repeatedly subjected to high temperatures and loads [2]. Toughness and yield strength, determined by the martensite and carbides [3,4], are the most important mechanical properties of H13 [5].

Most carbides dissolve in H13 during the quenching process and precipitate from martensite as uniformly dispersed nanoparticles during tempering, resulting in secondary hardening. Thus, the heat treatment process has significant effects on the properties of the carbides and hence on the quality of the steel. Extensive research has been performed on both the solidification process in H13 and the effects of heat treatment; changes in the microstructure and categories of carbides have been studied in the laboratory and also at the industrial plant scale [6–8]. By electrolytically extracting precipitates after tempering H13, Song et al. [9] discovered that the carbides in H13 were mainly V_8C_7, which not only includes pseudo-eutectic carbides not dissolved in H13 during forging, but also includes the secondary hardening carbides precipitated from martensite. These secondary carbides are regarded as the main strengthening phase because of their fine particle size and well-dispersed distribution. In addition, M_2C, M_6C, and M_7C_3-type carbides also precipitate during tempering. Zhang et al. [10] measured the

particle distribution of MC by using small-angle X-ray scattering and reported that the precipitation strengthening increment of tempering at 873 K was 171.72 MPa. Fu et al. [11] demonstrated that the precipitation strengthening increments of Fe_3C and Ti(C,N) during rapid cooling after rolling were 194.4 MPa and 130 MPa, respectively, in Ti microalloyed high-strength weathering steel. These reports, however, did not precisely describe the shape, size, and distribution of the carbides. The influence of precipitates on the mechanical properties—especially toughness and yield strength—of hot work die steel is also rarely reported.

A previous study by our group [12] investigated the effect of different heat treatments on the precipitates and strengthening mechanism in H13, and a root-mean-square summation law, which was confirmed as the most applicable for H13 steel, was summarized as $\sigma = \sigma_g + \sigma_s + (\sigma_d^2 + \sigma_p^2)^{\frac{1}{2}}$, where σ_g, σ_s, σ_d and σ_p represent the contributions of fine-grain strengthening, solid-solution strengthening, dislocation strengthening, and precipitates' strengthening.

In this article, the types of carbides formed in H13 during tempering are described, their characteristics are clarified, and then thermodynamic calculations are performed. The type, size, and volume of carbides are analyzed in three different regions of the H13 ingot, and their contribution to the yield strength is discussed. The influence of precipitates on yield strength and impact properties is also discussed.

2. Experimental Materials and Methods

The chemical composition of H13 hot work die steel is shown in Table 1. The smelting process included electric arc furnace (EAF) melting, ladle refining (LF), vacuum degassing (VD), and electro-slag remelting (ESR). The ingot diameter was 220 mm and its available weight was up to 5 t.

Table 1. Chemical composition of H13 steel, %.

C	Si	Mn	P	S	Cr	Ni	Cu	Mo	V	Al	N	T [O]
0.39	0.88	0.34	0.0064	0.0005	5.13	0.086	0.054	1.5	0.99	0.047	0.0015	0.0017

The heat treatment was simulated industrial processing and was performed as follows:

First, the ESR ingot was forged at 1373 K to bar stock with a diameter of 105 mm. Then the forged ingot was annealed at 1133 K for 10 h, cooled to 773 K in the furnace, and further cooled to room temperature in air, as shown in Figure 1a.

Next, a 105 mm diameter × 60 mm thick sample was cut from the central part of the ingot. This sample was preheated to 1113 K at a rate of 13 K/min, maintained for 20 min, heated to 1303 K at a rate of 6 K/min, maintained for an additional 30 min, and then cooled in oil at 33 K/min, as shown in Figure 1b.

Finally, the sample was tempered for 2 h at 863 K, and then cooled in air to room temperature, as shown in Figure 1c.

Smaller samples were then cut from the main sample for transverse and longitudinal impact value (Charpy V-notch) tests, tensile strength measurements, and metallographic studies. The dimensions of the Charpy test samples were 10 × 10 × 55 mm^3, the tensile test samples were Φ8 × 120 mm^2 (the gripping end was Φ12 × 50 mm^2), and the metallographic samples were 10 × 10 × 10 mm^3. The positions of sampling were: near the center (#1), halfway between the center and the outer surface (hereafter referred to as "half-radius") (#2), and near the outer surface (#3) of the H13 ingot, as shown in Figure 2.

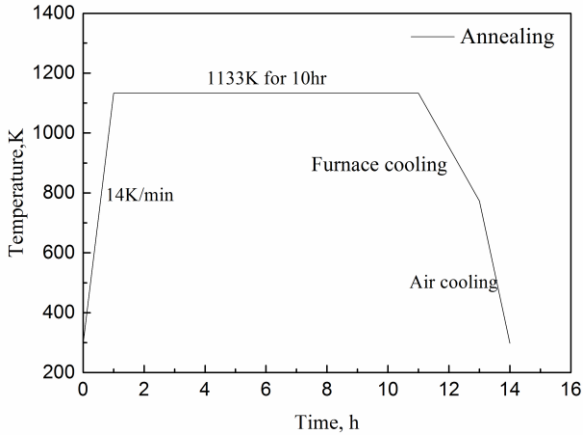

(**a**) Annealing

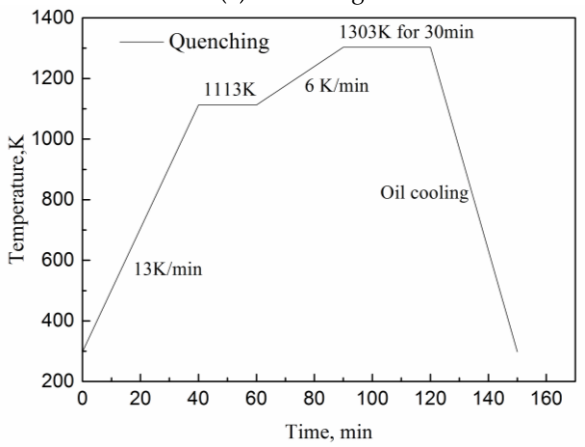

(**b**) Quenching

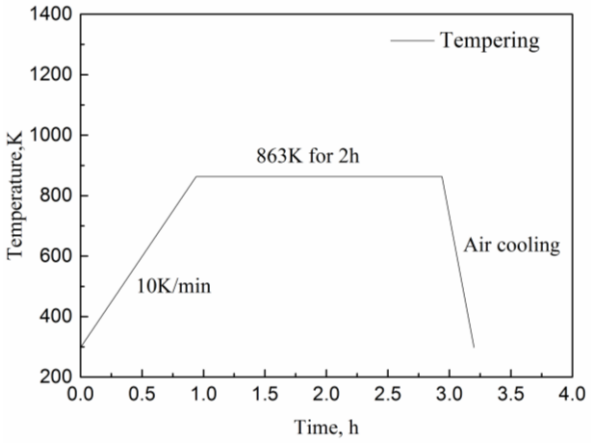

(**c**) Tempering

Figure 1. Heat treatment for the H13 ingot after forging. (**a**) Annealing; (**b**) Quenchin; (**c**) Temperin.

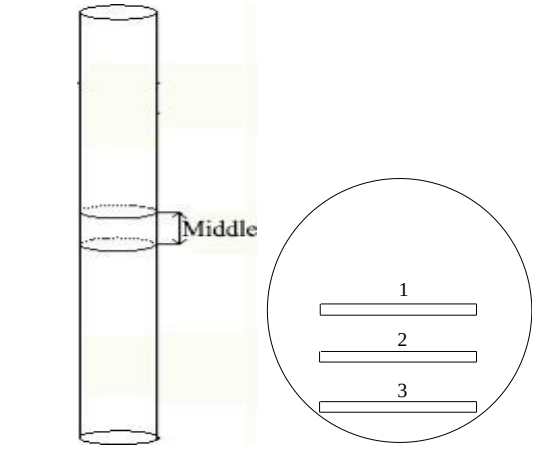

(**a**) Large sample (**b**) Specific position

Figure 2. Positions of the H13 steel samples: (**a**) Large sample taken from the middle of the ingot after annealing; (**b**) Individual test samples taken from the center (#1), half-radius (#2), and outer surface (#3) of (**a**) after tempering.

The impact values of the three samples were tested by a ZBC2452-B Pendulum impact testing machine (MTS System Corporation, Shenzhen, China). Tensile strength, yield strength, elongation, and area reduction were examined with a CMT4105 electronic universal testing machine (MTS System Corporation, Shenzhen, China). A 500MRA Rockwell hardness tester was used to measure the hardness of the samples. The microstructure of the steel was observed with a 9XB-PC optical microscope (Shanghai Optical Instrument Factory, Shanghai, China). The morphology of the carbides in the three samples was examined with an F30 high resolution transmission electron microscope (HR TEM) (FEI Company, Hillsboro, OR, USA). The carbon extraction replica method was used to prepare the TEM samples; the specific steps were as follows: first etch the polished metallographic samples in 8% nitric acid alcohol solution, then coat them with a layer of evaporated carbon film, approximately 20–30 nm thick, and finally extract the precipitates by using 10% nitric acid alcohol solution and mount the carbon membrane on a copper grid. The morphology of the precipitates was analyzed by TEM after the samples were dried.

3. Experimental Results

3.1. Metallographic Structure after Tempering

As shown in Figure 3, the microstructure of H13 after tempering includes martensite, fine-grained pearlite, and a large number of carbides. The heterogeneity of the microstructures is obvious both at the center and at the half-radius of the ingot (Figure 3a,b). Light field represents the alloy-rich and carbide-rich field, while the situation is opposite in the dark field where the carbides dissolve and martensite forms [13]. Especially in the center, there exist segregation bands composed of eutectic carbides, as shown in Figure 3a. Compared with the center and the half-radius of the ingot, the microstructures near the outer surface (Figure 3c) are much more homogeneous and appear to have the narrowest martensite laths.

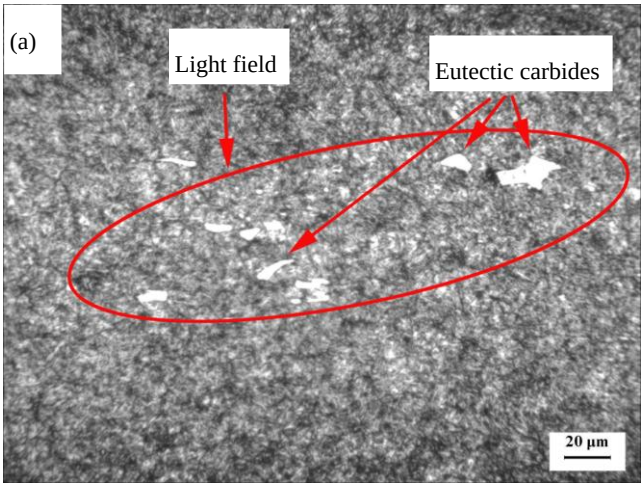

(a) Center

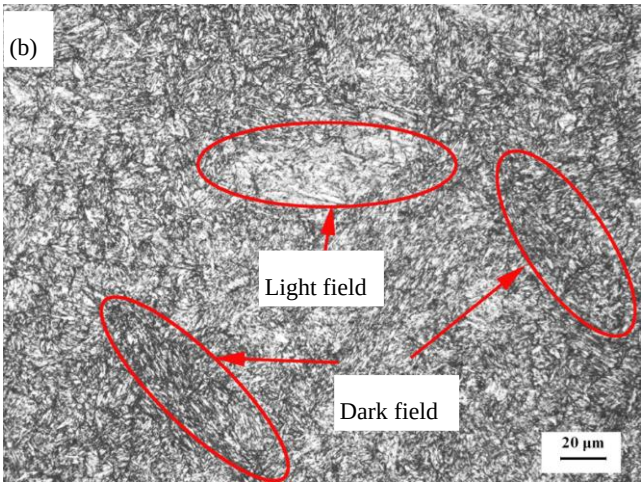

(b) Half-radius

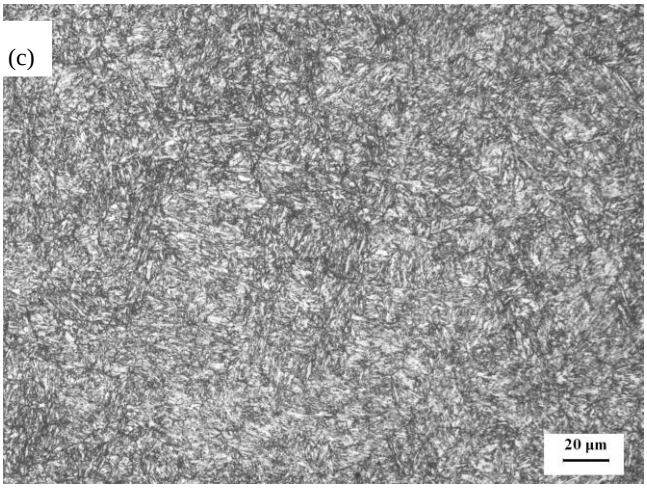

(c) Outer surface

Figure 3. Microstructure of the H13 ingot at different positions after tempering. (**a**) Center; (**b**) Half-radius; (**c**) Outer surface.

It is well known that the cooling speed is lowest in the center and fastest at the surface during ESR [14]. It is difficult to eliminate eutectic carbides and segregation during ESR by conventional heat

treatment. Thus, the formation of eutectic carbides consumes alloying elements and carbon in H13, influencing the formation of nanocarbides; meanwhile, the segregation that causes the heterogeneous distribution of elements in H13 can in some cases also have an effect on the distribution, sizes, and amounts of nanocarbides.

3.2. Types of Precipitates during Tempering

After observing 300 photomicrographs (14.5 × 14.5 μm^2 each) as well as the EDS results, it was determined that most of the fine particles are V-rich MC-type carbides along with some Mo-rich carbides, usually squares or elongated in shape and smaller than 200 nm, as shown in Figures 4a and 5a. Some Cr-rich carbides were also observed; these are usually larger than the V- and Mo-rich carbides—200 nm or more—and are irregularly spherical in shape. As shown in Figures 4 and 6, V_8C_7 was found near the surface of the H13 ingot, and $M_{23}C_6$ was also detected [15]. However, most of the $M_{23}C_6$ was found at the center of the H13 ingot in this experiment. V_8C_7 belongs to the family of cubic MC-type carbides, and its lattice constant is $a = b = c = 0.833$ nm. The particles found near the surface of our H13 ingot were approximately spherical in shape, with a diameter of about 100 nm.

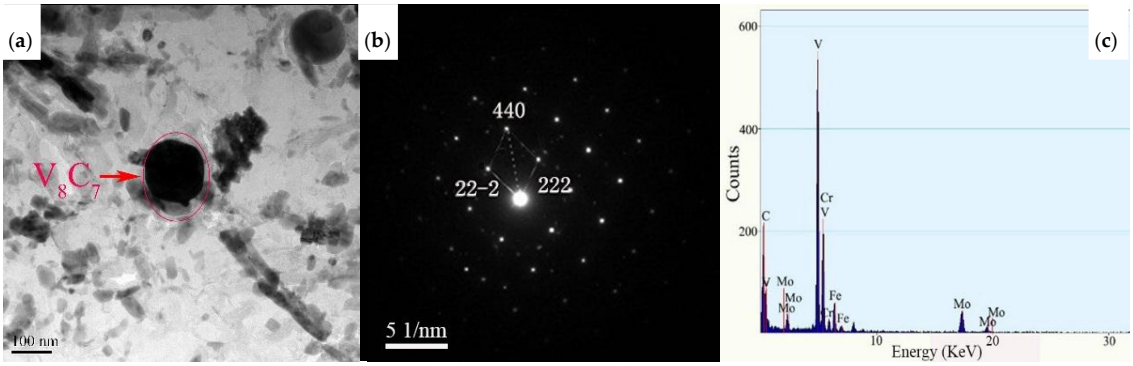

Figure 4. Precipitates of V_8C_7 near the surface of the H13 ingot after tempering: (**a**) Morphology by TEM; (**b**) SAED (Selected Area Electron Diffraction) analysis; (**c**) EDS (Energy Dispersive X-ray Spectrum) analysis.

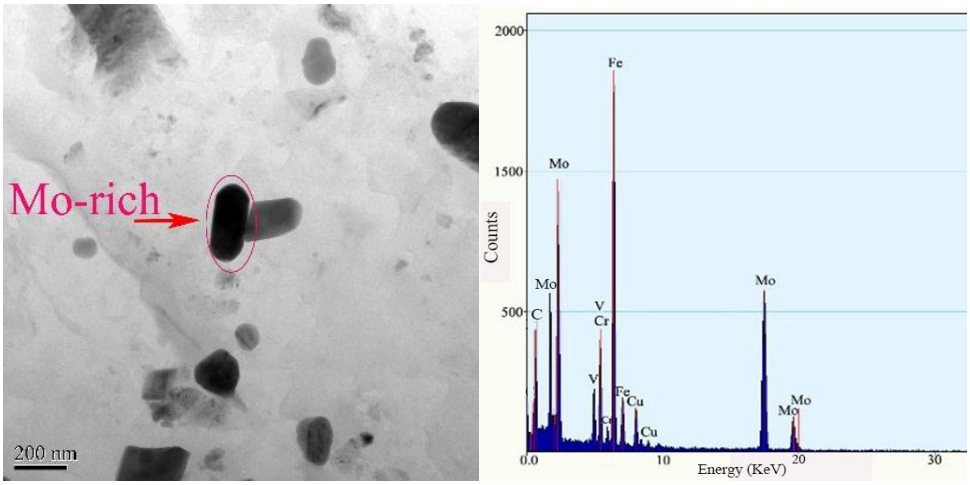

(**a**) (**b**)

Figure 5. Precipitates of Mo-rich carbides at half-radius of the H13 ingot after tempering: (**a**) Morphology by TEM; (**b**) EDS analysis.

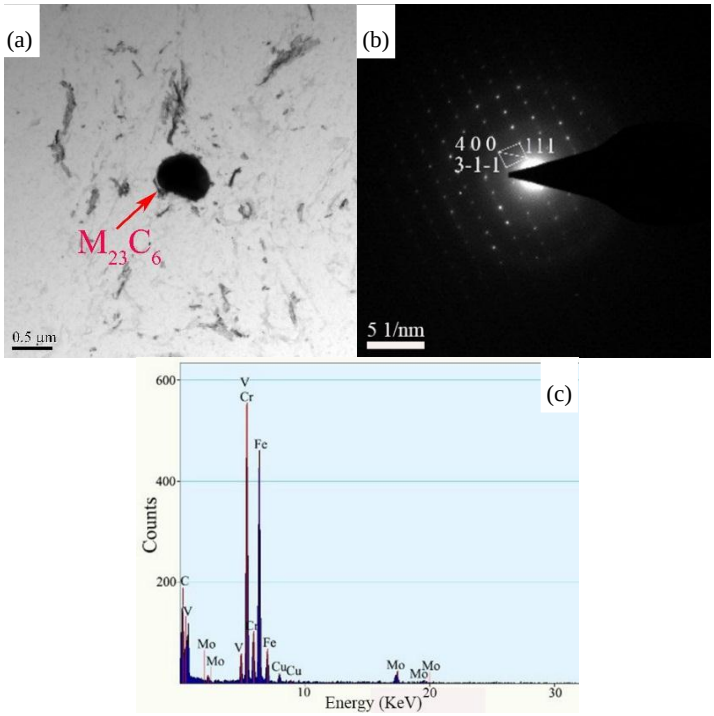

Figure 6. Precipitates of $M_{23}C_6$ at the center of the H13 ingot after tempering: (**a**) Morphology by TEM; (**b**) SAED analysis; (**c**) EDS analysis.

According to the morphology and EDS analysis in Figure 5, the indicated nanoparticle is an M_6C-type carbide, which is detected at the half-radius of the H13 ingot, rich in Mo and Fe, with an elongated shape, about 200 × 90 nm^2.

The types of precipitates that were found in H13 by using the carbon extraction replica method were consistent with the published literature [7,9]. It was also found in this experiment that although the size of the Mo-rich M_6C particles was larger than that of the V-rich MC, both of them are widely and uniformly distributed throughout the ingot, and both work as secondary hardening and contribute to tempering resistance. V-rich MC, mixed with M_2C and M_6C in steel, can improve the tempering resistance [16].

3.3. Analysis of the Size and Volume of Precipitate Carbides

In the present trials, 15 large fields of view (6000×) and 15 small fields of view (30,000×) were randomly selected from points #1, #2, and #3 in order to analyze the volumes and size distribution of the carbides. Figure 7a,b shows the micro-morphology and distribution of carbides in H13 after tempering for 2 h.

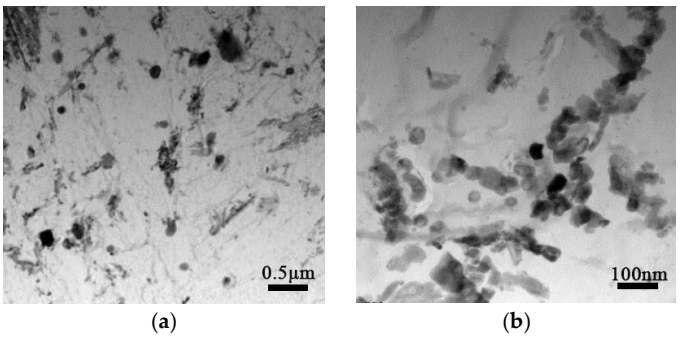

(**a**) (**b**)

Figure 7. Distribution of carbides at the half-radius of the H13 ingot after tempering. (**a**) Large field of view; (**b**) Small field of view.

The amount of precipitates and their size distribution were obtained by using Image-Pro Plus software (Media Cybernetics Inc., Rockville, MD, USA). Image-Pro Plus is designed for processing, enhancing, and analyzing pictures; it has exceptionally rich measurement and customization features. The statistical results are listed in Table 2.

Table 2. Statistics of precipitates at different positions in H13 after tempering.

Sample Number	Visual Field Area/μm^2	Field Number	Number of Precipitates	Average Size/nm
1	3.8 × 3.8 0.8 × 0.8	15 15	711 394	82.6
2	3.8 × 3.8 0.8 × 0.8	15 15	815 327	81.6
3	3.8 × 3.8 0.8 × 0.8	15 15	683 261	60.7

Table 2 shows the quantity and size distribution of the carbides. It can be seen that the sizes of the precipitation carbides decrease gradually from the center to the surface of the H13 ingot, while the precipitation quantity is largest at the half-radius. The average size of the nanocarbides at the center is almost the same as that at the half-radius. Under the influence of eutectic carbides and the segregation of metallic elements, nanocarbides precipitate insufficiently; therefore, the precipitation quantity at the center is smaller than that at the half-radius after tempering. Many fine carbides on the surface, such as M_2C, do not have enough time to precipitate because of the rapid oil cooling speed after tempering; therefore there are very few carbides near the surface. However, near the surface, the average size of carbides is 60.7 nm; this size is finer than the corresponding sizes at either the center or at the half radius. In order to obtain H13 steel with sufficiently high strength and hardness, the appropriate holding time and temperature should be set to allow for sufficient nanocarbides to precipitate.

The precipitation quantities in different particle size ranges (<150 nm) of these three positions is shown in Figure 8, and it can be seen that:

(1) The carbides less than 150 nm in size precipitate most frequently at the half-radius of the H13 ingot. Therefore, the quantity of precipitates at this position is the largest.
(2) The greatest number of carbides are of sizes less than 50 nm, occurring near the surface of the ingot. Therefore, the average size is smallest at this position.
(3) The particle size distribution deviates from a Gaussian distribution, possibly because short-time tempering leads to insufficient growth of the precipitates and a large number of small newly-formed carbides precipitate during tempering.

It can be concluded that, after tempering for 2 h, the carbides had an average size of 76 nm, which is finer than the size after ESR (90 nm), forging annealing (206 nm), and quenching (137 nm) [17,18]. Although the residual carbides grow and coarsen at lower temperatures during quenching [7], martensite decomposes and secondary phases are precipitated during tempering; thus a large number of nanocarbides, which have a significant effect on precipitation strengthening, precipitate from the grain boundaries and inside the grains of martensite. Therefore, the quantity increases and the average size decreases significantly, as shown in Table 2.

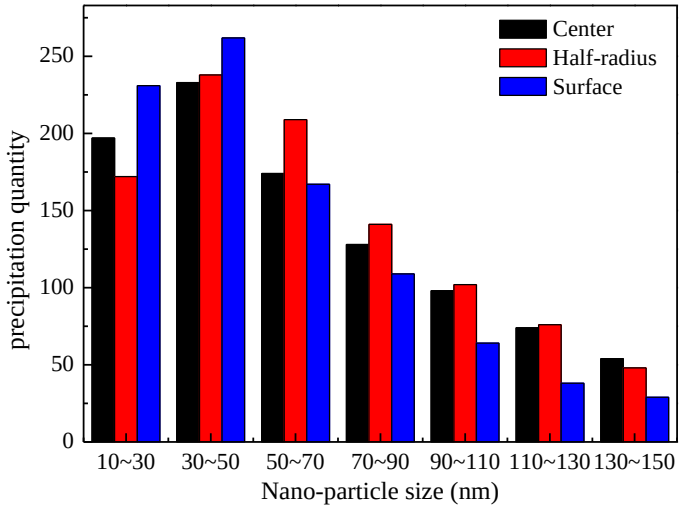

Figure 8. Size distribution of carbides in H13 at the three different locations after tempering.

4. Discussion

4.1. Thermodynamic Calculation of Carbides during Tempering

As mentioned above, MoC, VC, and V_8C_7 belong to the MC family of carbides; and $M_{23}C_6$ is a Cr-rich carbide. The following study focuses on the precipitation temperatures of VC, V_8C_7, $Cr_{23}C_6$, and MoC, and their evolution during tempering is also discussed.

According to the relevant chemical reaction and Gibbs free energy [19–21], a precipitation reaction of $Cr_{23}C_6$ and MoC is obtained.

$$23[\mathrm{Cr}]_\gamma + 6[\mathrm{C}]_\gamma = \mathrm{Cr_{23}C_6(s)}, \Delta G^\varnothing = -959797.2 + 1172.7T \quad (1)$$

$$[\mathrm{Mo}]_\gamma + [\mathrm{C}]_\gamma = \mathrm{MoC(s)}, \Delta G^\varnothing = -149038 + 94.97T \quad (2)$$

The equilibrium solubility product in austenite is obtained from Equations (1) and (2).

$$\ln\left(w[\mathrm{Cr}]_\%^{23} \cdot w[\mathrm{C}]_\%^{6}\right)_\gamma = 141.05 - \frac{115443.49}{T} \quad (3)$$

$$\ln\left(w[\mathrm{Mo}]_\% \cdot w[\mathrm{C}]_\%\right)_\gamma = 11.42 - \frac{17926.15}{T} \quad (4)$$

Owing to the very low solubility of MC-type carbides in austenite, it is difficult to test the solubility of MC-type carbides experimentally, and the only result available at the present time has been deduced from thermodynamic data. According to the published literature [21], the solubility products of V_8C_7 and VC in ferrite and austenite are given by the following:

$$\ln\left(w[\mathrm{V}]_\% \cdot w[\mathrm{C}]_\%^{0.875}\right)_\alpha = 13.01 - \frac{21510.02}{T} \quad (5)$$

$$\ln\left(w[\mathrm{V}]_\% \cdot w[\mathrm{C}]_\%\right)_\gamma = 15.48 - \frac{21878.5}{T} \quad (6)$$

The precipitation temperatures of these carbides can be obtained by inserting the following values into Equations (3)–(6): $w[\mathrm{Cr}]_\% = 5.13$, $w[\mathrm{Mo}]_\% = 1.5$, $w[\mathrm{V}]_\% = 0.99$, and $w[\mathrm{C}]_\% = 0.39$; the results are listed in Table 3.

Table 3. Precipitation temperatures of carbides in H13 during solidification.

Austenite Region				
Carbides	V_8C_7	MoC	VC	$Cr_{23}C_6$
Temperature	1553.5 K	1499.0 K	1331.8 K	1058.2 K

Only when the temperature is below the precipitating temperatures do these carbides precipitate. The austenite region of H13 is between the liquid line at 1755 K and the A_{r1} line at 1048 K [1]. From Table 3, the precipitation sequence is MC > $M_{23}C_6$.

According to experimental results combined with theoretical calculations, it can be concluded that V_8C_7 precipitates at a higher temperature (1553.5 K), but it has low coarsening speed (Figure 4). V-rich carbides are more widely dispersed and finer than Cr carbides. Another conclusion is that $M_{23}C_6$ precipitates at a lower temperature (1058.2 K), but has a faster coarsening speed (Figure 5), because the diffusion rate of Cr in austenite is greater than that of V [21]. $M_{23}C_6$ has high Cr content and thus Cr-rich carbides are easy to grow at the grain boundaries [22]. Cr carbides have a larger precipitation volume fraction and are not so widely distributed in the form of fine particles. MoC precipitates are not stable at high temperature (<1040 K), and they are easier to combine with Fe and Cr to form M_6C [1].

In actual circumstances, carbon and alloy segregation always exists, so the precipitation temperature of carbides will fluctuate in different regions.

4.2. Effect of Precipitates in H13 during Tempering on Mechanical Properties

The mechanical properties of H13 after 2 h tempering are shown in Table 4.

Table 4. Tensile property and hardness of different positions in H13 after tempering.

Sample Number	Tensile Strength, R_m (MPa)	Yield Strength, R_p (MPa)	Elongation, A (%)	Area Reduction Rate, Z (%)	HRC
Center, #1	1764.6	1456.0	7.0	30.6	49.2
Half-radius, #2	1743.1	1426.4	8.9	28.9	47.5
Surface, #3	1750.2	1436.0	8.0	35.1	46.2

According to the theory of precipitation strengthening [21], when a large number of fine nanocarbides precipitate during tempering, the strength of the steel increases because of the decomposition of martensite. Although a large number of precipitates may cause a decrease in plasticity, the reduction in alloying element content and decrease in dislocation density may improve the plasticity [23–25]. As shown in Table 4, the strength and plasticity after tempering are almost independent of the sample position. However, the hardness seems to be lower from the center to the surface, showing that the ingot was heated unevenly.

From the size distribution of Figure 8, it can be seen that the average size of precipitates is larger than 10 nm; therefore, the bypass mechanism has the main effect on precipitation strengthening [11]. In order to calculate the contribution of the precipitates to yield strength, we employed segment calculation and summation of the results (Table 5). According to the methods of McCall-Boyd [26] and the Ashby-Orowan correction model [27], the formula for the volume fraction and precipitation strengthening of the precipitates in H13 is obtained as Formulas (12) and (13). McCall and Boyd [28] analyzed the characteristics of precipitates in ThO_2 by employing carbon extraction replica methods in the 1960s. The McCall-Boyd method is an accurate way to calculate the volume fraction of precipitates with uneven distribution in alloys.

Table 5. Size, volume, and calculation of precipitation strengthening in H13 of different positions after tempering for 2 h.

Size (nm)	Amount			Average Diameter, D (nm)			Volume Fraction, f			Average Radius, r (nm)			Yield Strength Increment, τ_P (MPa)		
	1#	2#	3#	1#	2#	3#	1#	2#	3#	1#	2#	3#	1#	2#	3#
10–30	197	172	231	21.79	21.73	21.74	0.00015	0.00013	0.00035	10.90	10.87	10.87	26.78	25.01	40.88
30–50	233	238	262	40.27	40.44	39.31	0.00061	0.00063	0.0013	20.14	20.22	19.66	33.86	34.25	50.36
50–70	174	209	167	59.22	59.12	58.66	0.00099	0.0012	0.0019	29.61	29.56	29.33	31.82	34.87	43.89
70–90	128	141	109	79.67	79.1	79.67	0.0013	0.0014	0.0022	39.84	39.55	39.84	28.99	30.38	37.73
90–110	98	102	64	98.43	99.01	99.86	0.0015	0.0016	0.0021	49.22	49.51	49.93	26.42	26.99	30.20
110–130	74	76	38	118.74	118.15	120.02	0.0017	0.0017	0.0018	59.37	59.08	60.01	23.77	24.07	24.08
130–150	54	48	29	139.54	138.94	139.2	0.0017	0.0015	0.0018	69.77	69.47	69.60	20.91	19.70	21.60
150–170	38	53	17	160.42	159.11	157.63	0.0016	0.0022	0.0014	80.21	79.56	78.82	17.97	21.19	16.90
170–190	26	35	9	178.54	177.69	180.89	0.0013	0.0018	0.00095	89.27	88.85	90.45	15.14	17.55	12.59
190–210	24	26	6	200.26	198.01	199.23	0.0016	0.0017	0.00077	100.13	99.01	99.62	14.83	15.41	10.45
210–230	15	11	4	218.68	220.87	222.11	0.0012	0.00087	0.00064	109.34	110.44	111.06	11.90	10.20	8.69
230–250	11	11	4	242.57	239.75	238.34	0.0011	0.0010	0.00074	121.29	119.88	119.17	10.36	10.34	8.79
250–270	12	9	1	260.18	259.54	254.88	0.0013	0.00099	0.00021	130.09	129.77	127.44	10.94	9.47	4.44
270–290	5	6	2	275.09	278.86	278.88	0.00062	0.00076	0.00050	137.55	139.43	139.44	7.13	7.82	6.37
290–310	5	1	0	294.86	307.76	0	0.00071	0.00015	0	147.43	153.88	0	7.21	3.24	0
310–330	4	1	1	320.86	316.7	313.36	0.00067	0.00016	0.00032	160.43	158.35	156.68	6.53	3.26	4.59
330–350	5	2	0	340.15	334.18	0	0.00094	0.00036	0	170.08	167.09	0	7.37	4.65	0
350–370	2	1	0	357.39	353.43	0	0.00042	0.00020	0	178.70	176.72	0	4.69	3.31	0
Total	1105	1142	944				0.0193	0.0184	0.0169				279.84	301.72	321.56

$$f_i = \left(\frac{1.4\pi}{6}\right) \cdot \left(\frac{N_i D_i^2}{A}\right) \quad (7)$$

$$\sigma_s = \sum_{i=1}^{n} \sigma_i = \sum_{i}^{n} [\frac{10\mu b}{5.72\pi^{3/2} r_i} f_i^{\frac{1}{2}} \ln(\frac{r_i}{b})] \quad (8)$$

Here, A represents the area of the photos in μm^2; N_i represents the amounts of precipitates within a certain range; D_i represents the average diameter in nanometers for precipitates within a certain range; r_i represents the average radius in nanometers for precipitates within a certain range; f_i represents the volume fraction, in % of precipitates within a certain range; μ represents a shearing factor (80.26×10^3 MPa for steel); and b represents the Burgers Vector, with a value of 2.48×10^{-4} μm.

The volume fraction of precipitates and the increment of precipitation strengthening in the three different positions of H13 after tempering are calculated according to Formulas (7) and (8). The calculation process is listed in Table 5, and the results of the calculations are listed in Table 6.

Table 6. Contribution to yield strength of the precipitates in H13 after tempering.

Item	Center (1#)	Half-Radius (2#)	Surface (3#)
Average size (nm)	82.6	81.6	60.7
Volume fraction (%)	1.9	1.8	1.7
Contribution to the yield strength (MPa)	279.8	301.7	321.6
Actual yield strength (MPa)	1456.0	1426.4	1436.0
The proportion of yield strength attributable to precipitation strengthening (%)	19.2	21.2	22.4

From Table 6, combined with Figure 9, it can be seen that the contribution of precipitates to the yield strength increases as the average size of the precipitates becomes finer, and the volume fraction decreases from the center to the surface of the H13 ingot after 2 h tempering.

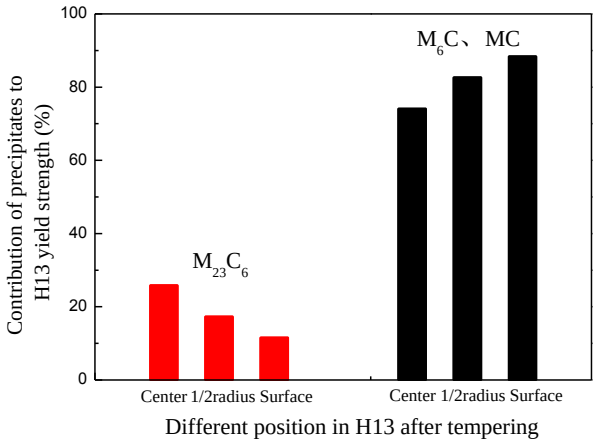

Figure 9. Contribution to yield strength of different types of carbides in different positions in H13 after tempering.

After tempering for 2 h, the contribution of nanoprecipitates to the yield strength of H13 remains at about 300 MPa. The average diameter and total volume fraction of precipitates are 60–83 nm and 1.7%–1.9%, respectively. The measured results of yield strength show little difference between the three positions. It was also found that the surface of H13 has the finest precipitates, and experiences the

largest precipitation strengthening of H13. Combining the information from Section 3.2 and Table 5, the contribution of different types of carbides to yield strength is summarized in Figure 9.

From Figure 9, it can be seen that MC and M_6C have a stronger strengthening effect than $M_{23}C_6$ on H13 yield strength, contributing 74%–88% of precipitation strengthening. From the center to the surface of the H13 ingot, the contribution of $M_{23}C_6$ to the yield strength decreases, while the contribution of MC and M_6C to the yield strength increases. It can be concluded that MC and M_6C are the main carbides in precipitation strengthening. These carbides have good tempering stability as their average size is below 200 nm.

The transverse and longitudinal impact values at the center, half-radius, and surface of H13 after tempering for 2 h are shown in Figure 10.

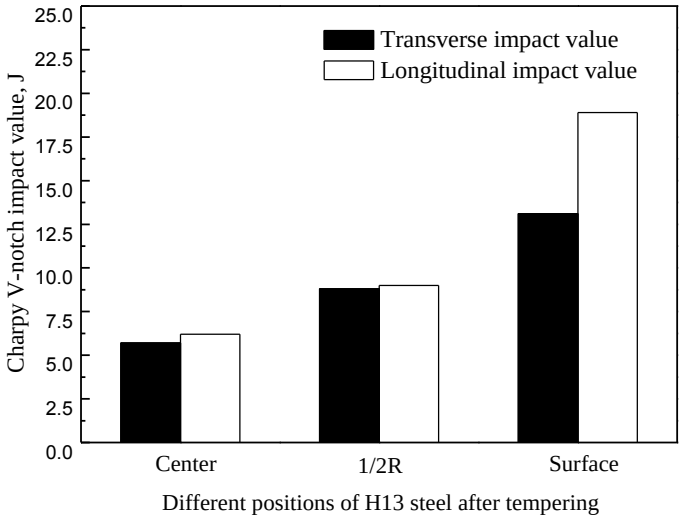

Figure 10. Impact values in different positions of H13 after tempering.

From Figure 10, the impact values after tempering become better from the center of the ingot to its outer surface. It can be seen that the toughness was the lowest at the center of the ingot. One reason is the formation of ribbon segregation and eutectic carbides in the center during ESR [12]. The other reason is that the volume fraction of the precipitates decreases, especially the dissolution of $M_{23}C_6$ [22] and the precipitation of MC, M_6C during tempering (Figure 9).

In conclusion, it is the homogeneous structure and fine precipitates with moderate distribution that improve the toughness of H13.

5. Conclusions

1. Microstructures near the surface of the H13 ingot are homogeneous and have the narrowest martensite laths.
2. V-rich MC, Mo-rich M_6C, and Cr-rich $M_{23}C_6$ are the main kinds of carbides that precipitate in H13 during tempering. The shapes of MC and M_6C are approximately square or elongated and their sizes are less than 200 nm. The shape of $M_{23}C_6$ is irregularly spherical and its size is greater than 200 nm. From thermodynamic calculations, the precipitation sequence is MC > $M_{23}C_6$.
3. Carbide size and volume fraction decrease from the center to the periphery of H13 during tempering. There are more precipitates at the half-radius of H13 than that at the center. The surface of the H13 ingot has the fewest precipitates.
4. The strength and plasticity after tempering are almost independent of the sample position. However, the hardness seems to be lower from the center to the surface, showing that the ingot was heated unevenly. The impact values after tempering become better from the center of the

ingot to its outer surface, because the compositions and structures are uniform near the surface of the ingot, and the precipitates are uniformly dispersed with the finest size.

5. The contribution of precipitation strengthening to yield strength increases from the center to the outer surface of the H13 ingot. The fraction of yield strength attributable to precipitation strengthening is 19.2%–22.4% after tempering. With a decreased contribution of $M_{23}C_6$ to precipitation strengthening, the contribution of MC and M_2C increases from the center to the surface. MC and M_6C have the main effect on precipitation strengthening in H13 after tempering, increasing the strength by up to 74.2%–88.4%.

Acknowledgments: The authors would like to express gratitude and appreciation to the National Natural Science Foundation of China (Grant No. 51274031) titled "Investigation on nanoscale precipitates in hot work die steel and comprehensive strengthening mechanism of steel". This study is also supported by the Beijing Key Laboratory of Special Melting and Preparation of High-end Metal Materials. Foundation Item: Supported by National Natural Science Foundation of China (No. 51274031)

Author Contributions: Angang Ning and Hanjie Guo conceived and designed the experiments; Angang Ning and Wenwen Mao performed the experiments; Angang Ning analyzed the data and wrote the paper; Jing Guo improved the English writing.

Conflicts of Interest: The authors declare no conflict of interest.

References

1. Feng, X.Z. *Mold Steel and Heat Treatment*; Machinery Industry Press: Beijing, China, 1984.
2. Sjöström, J.; Bergström, J. Thermal fatigue testing of chromium martensitic hot-work tool steel after different austenitizing treatments. *J. Mater. Process. Technol.* **2004**, *153–154*, 1089–1096. [CrossRef]
3. Pan, X.H.; Zhu, Z.C. The study of chemical composition and improvement and development for the H13 hot work die & mold steel. *Mold Manuf.* **2006**, *4*, 78–85.
4. Fuchs, K.D. Hot-work tool steels with improved properties for die casting applications, The use of tool steels: Experience research. In Proceedings of the 6th International Tooling Conference, Karlstad, Sweden, 10–13 September 2002; pp. 15–22.
5. Kheirandish, S.; Noorian, A. Effect of niobium on microstructure of cast AISI H13 hot work tool steel. *J. Iron Steel Res. Int.* **2008**, *15*, 61–66. [CrossRef]
6. Ma, D.S.; Zhou, J.; Chen, Z.Z.; Zhang, Z.K.; Chen, Q.A.; Li, D.H. Influence of thermal homogenization treatment on structure and impact toughness of H13 ESR steel. *J. Iron Steel Res. Int.* **2009**, *16*, 56–60. [CrossRef]
7. Hu, X.B.; Li, L. Changes of morphology and composition of carbides in H13 steel after thermal fatigue. *Trans. Mater. Heat Treat.* **2007**, *28*, 82–87.
8. Mebarki, N.; Delagnes, D.; Lamesle, P.; Delmas, F.; Levaillant, C. Relationship between microstructure and mechanical properties of a 5% Cr tempered martensitic tool steel. *Mater. Sci. Eng. A* **2004**, *387–389*, 171–175. [CrossRef]
9. Song, W.W.; Min, Y.A.; Wu, X.C. Study on carbides and their evolution in H13 hot work steel. *Trans. Mater. Heat Treat.* **2009**, *30*, 122–126.
10. Zhang, K.; Yong, Q.L.; Sun, X.J.; Li, Z.D.; Zhao, P.L.; Chen, S.D. Effect of tempering temperature on microstructure and mechanical properties of high Ti microalloyed directly quenched high strength steel. *Acta Metall. Sin.* **2014**, *50*, 913–920.
11. Fu, J.; Li, G.Q.; Mao, X.P.; Fang, K.M. Nanoscale cementite precipitates and comprehensive strengthening mechanism of steel. *Metall. Mater. Trans. A* **2011**, *42A*, 3797–3812. [CrossRef]
12. Mao, W.; Ning, A.; Guo, H. Nanoscale precipitates and comprehensive strengthening mechanism in AISI H13 steel. *Int. J. Miner. Metall. Mater.* **2016**, *23*, 1056–1064. [CrossRef]
13. Zhou, J.; Ma, D.S.; Liu, B.S.; Kang, A.J.; Li, X.Y. Research of band segregation evolution of H13 steel. *J. Iron Steel Res.* **2012**, *24*, 47–57.
14. Li, Z.B. *Electroslag Metallurgy Equipment and Technology*; Metallurgical Industry Press: Beijing, China, 2012.
15. Guo, K.X.; Ye, H.Q.; Wu, Y.K. *Application of Electron Diffraction Pattern in Crystallography*; Science Press: Beijing, China, 1983.
16. Gong, X.M. *Fundamentals and Applications of Phase Transition Theory*; Wuhan University of Technology Press: Wuhan, China, 2004.

17. Ning, A.G.; Guo, H.J.; Chen, X.C.; Sun, X.L. Precipitation behaviors of carbides in H13 steel during ESR, forging and tempering. *J. Univ. Sci. Technol. Beijing* **2014**, *36*, 895–902.
18. Ning, A.G.; Mao, W.W.; Guo, H.J.; Chen, X.C. Precipitation behaviors and strengthening of carbides in H13 steel during quenching. *Chin. J. Process Eng.* **2014**, *14*, 86–92.
19. Ye, D.L.; Hu, J.H. *Practical Inorganic Thermodynamic Data Manual*, 2nd ed.; Metallurgical Industry Press: Beijing, China, 2002.
20. Chen, J.X. *Steelmaking Common Chart Data Manual*, 2nd ed.; Metallurgical Industry Press: Beijing, China, 2010.
21. Yong, Q.L. *The Second Phase of the Steel Materials*; Metallurgical Industry Press: Beijing, China, 2006.
22. Klimiankou, M.; Lindau, R.; Moslang, A. Direct correlation between morphology of $(Fe,Cr)_{23}C_6$ precipitates and impact behavior of ODS steels. *J. Nucl. Mater.* **2007**, *367–370*, 173–178. [CrossRef]
23. Oikawa, T.; Zhang, J.J.; Enomoto, M.; Adachi, Y. Influence of carbide particles on the grain growth of ferrite in an Fe-0.1C-0.09V alloy. *ISIJ Int.* **2013**, *53*, 1245–1252. [CrossRef]
24. Garcia-Mateo, C.; Capdevila, C.; Caballero, F.G.; Andres, C.G.D. Influence of V precipitates on acicula ferrite transformation Part 1: The role of nitrogen. *ISIJ Int.* **2008**, *48*, 1270–1275. [CrossRef]
25. Cui, Z.Q.; Chun, Q.Y. *Metal Science and Heat Treatment*; Machinery Industry Press: Beijing, China, 2007.
26. Seher, R.J.; James, H.M.; Maniar, G.N. *Stereology and Quantitative Metallography, West Conshohocken*; Pellissier, G.E., Purdy, S.M., Eds.; ASTM International: West Conshohocken, PA, USA, 1972; pp. 119–137.
27. Kneissl, A.C.; Garcia, C.I.; Deardo, A.J. *HSLA Steels: Processing, Properties, and Applications*; Geoffrey, T., Zhang, S., Eds.; The Minerals, Metals and Materials Society: San Diego, CA, USA, 1992; pp. 99–102.
28. McCall, J.L.; Boyd, J.E. Proceedings International Metallographic Society, PIMTB. In Proceedings of the 1968 Annual Meeting, Boston, MA, USA, 21 July 1968.